7. Bu, X., Feng, P., Gier, T. E. & Stucky, G. D. Two ethylenediamine templated zeolite type structure sin zinc arsenate and cobalt phosphate systems. *J. Solid State Chem.* **136,** 210–215 (1998).
8. Smith, J. V. Topochemistry of zeolites and related materials. 1. Topology and geometry. *Chem. Rev.* **88,** 148–182 (1988).
9. Meier, W. M., Olson, D. H. & Baerlocher, C. *Atlas of Zeolite Structure Types* (Elsevier, Boston, 1996).
10. Bu, X., Feng, P. & Stucky, G. D. Large-cage zeolite structures with multidimensional 12-ring channels. *Science* **278,** 2080–2085 (1997).
11. Monnier, A. *et al.* Cooperative formation of inorganic–organic interfaces in the synthesis of silicate mesostructures. *Science* **261,** 1299–1303 (1994).
12. Andersson, S. & Jacob, M. *The Mathematics of Structures* (R. Oldenbourg, München, 1997).
13. Andersson, S., Hyde, S. T., Larsson, K. & Lidin, S. Minimal surfaces and structures: from inorganic and metal crystals to cell membranes and biopolymers. *Chem. Rev.* **88,** 221–242 (1988).
14. Nenoff, T. M. *et al.* Structural and chemical investigations of $Na_3(ABO_4)_3{\cdot}4H_2O$-type sodalite phases. *Inorg. Chem.* **33,** 2472–2480 (1994).
15. Harrison, W. T. A., Gier, T. E. & Stucky, G. D. Two lithium chloroberyllo(phosphate/arsenate) sodalites: $Li_4Cl(BePO_4)_3$ and $Li_4Cl(BeAsO_4)_3$. *Acta Crystallogr. C* **50,** 471–473 (1994).
16. Feng, P., Bu, X. & Stucky, G. D. Hydrothermal synthesis and structural characterization of zeolite analogue compounds based on cobalt phosphate. *Nature* **388,** 735–741 (1997).

Supplementary Information is available on *Nature*'s World-Wide Web site (http://www.nature.com) or as paper copy from the London editorial office of *Nature*.

Acknowledgements. This research was supported in part by the National Science Foundation and the Office of Naval Research. P.F. thanks the Materials Research Laboratory for a Corning Foundation Fellowship. All figures were generated using software programs from Molecular Simulations.

Correspondence and requests for materials should be addressed to G.D.S. (e-mail: stucky@chem.ucsb.edu).

Heterogeneous production of nitrous acid on soot in polluted air masses

M. Ammann*, M. Kalberer*†, D. T. Jost*, L. Tobler*, E. Rössler*, D. Piguet*, H. W. Gäggeler*† & U. Baltensperger*

** Paul Scherrer Institute, Laboratory of Radio- and Environmental Chemistry, CH-5232 Villigen, Switzerland*

† University of Bern, Department of Chemistry and Biochemistry, CH-3012 Bern, Switzerland

Polluted air masses are characterized by high concentrations of oxidized nitrogen compounds which are involved in photochemical smog and ozone formation. The OH radical is a key species in these oxidation processes. The photolysis of nitrous acid (HNO_2), in the morning, leads to the direct formation of the OH radical and may therefore contribute significantly to the initiation of the daytime photochemistry in the polluted planetary boundary layer. But the formation of nitrous acid remains poorly understood: experimental studies imply that a suggested heterogeneous formation process involving NO_2 is not efficient enough to explain the observed night-time build-up of HNO_2 in polluted air masses[1]. Here we describe kinetic investigations which indicate that the heterogeneous production of HNO_2 from NO_2 on suspended soot particles proceeds 10^5 to 10^7 times faster than on previously studied surfaces. We therefore propose that the interaction between NO_2 and soot particles may account for the high concentrations of HNO_2 in air masses where combustion sources contribute to air pollution by soot and NO_x emissions. We believe that the observed HNO_2 formation results from the reduction of NO_2 in the presence of water by C–O and C–H groups in the soot. Although prolonged exposure to oxidizing agents in the atmosphere is likely to affect the chemical activity of these groups, our observations nevertheless suggest that fresh soot may have a considerable effect on the chemical reactions occurring in polluted air.

There is strong evidence that the spatial and temporal distribution of HNO_2 throughout the planetary boundary layer (PBL) is governed by continuous formation and daytime photolysis, which result in pronounced diurnal cycles with night-time maxima of up to more than 10 parts per billion by volume (p.p.b.v.). Correlation analysis points to NO_2 as a source component, and typical NO_2 conversion rates inferred are $10^{-6}\,s^{-1}$ (refs 2–4). The gas phase reaction of OH radicals with NO may only contribute significantly to the very low HNO_2 levels found during the day. HNO_2 emitted directly from combustion processes, together with other oxidized nitrogen compounds and soot, is of minor importance[5]. Therefore, a heterogeneous process involving NO_2 has been suggested. The maximum surface area per unit volume, S/V, attributed to ground and airborne surfaces is $10^{-2}\,cm^{-1}$ and $10^{-5}\,cm^{-1}$, respectively, for typical mixing heights (minimum, 100 m during the night) in the PBL. These surfaces have been proposed to catalyse the reaction between NO_2 and H_2O to form nitric and nitrous acid (reaction (1)), but measured HNO_2 formation rates using different types of bulk surfaces (solid materials and aqueous solutions) were found to be two to five orders of magnitude smaller than the NO_2 to HNO_2 conversion rates inferred from atmospheric observations[1].

$$2NO_2 + H_2O = HNO_3 + HNO_2 \quad (1)$$

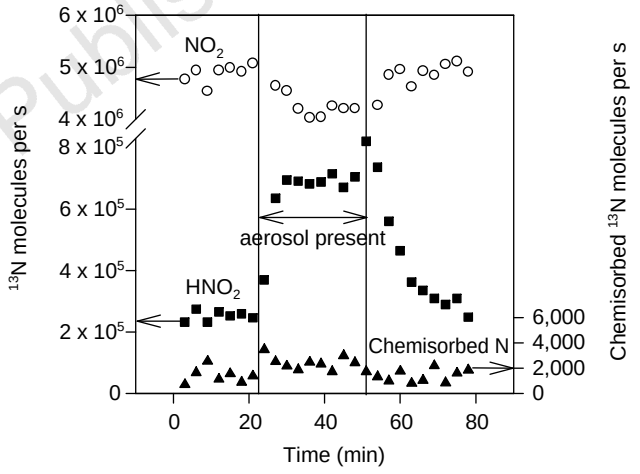

Figure 1 Online record of the rate of $H^{13}NO_2$ formation from 12 p.p.b.v. NO_2 in the absence and presence of soot particles. The data, obtained over a period of 80 min, record the rate of $H^{13}NO_2$ formation 20 s after two different gas flows have been mixed in a flow reactor at 22 °C, ambient pressure and 50% relative humidity. The first gas flow, containing NO_2 (enriched with $^{13}NO_2$) in He and 20% O_2, is introduced at a rate of $5\,cm^3\,s^{-1}$. The $^{13}NO_2$ content is adjusted so that the $^{13}NO_2$ molecules are fed into the reactor at a rate of $5 \times 10^6\,s^{-1}$. The NO_x-free soot aerosol is produced with a pulsed spark discharge between graphite rods in Ar, followed by dilution with air and a thermodenuder operating at 400 °C. O_2, N_2 and H_2O impurities in the Ar (99.998%) give rise to soot-like complex organic carbon compounds on the particle surfaces. Before introducing the gas mixture containing the aerosol into the reactor at a rate of $13.3\,cm^3\,s^{-1}$, part of the flow is passed through a differential mobility analyser coupled to a condensation particle counter to monitor the concentration and size distribution of the aerosol. The total flow rate through the 80-cm-long glass reactor (2.5 cm inner diameter) is $18.3\,cm^3\,s^{-1}$, and the gas mixture contains 14% O_2, 47% N_2, 13% He, 26% Ar, 1.2% H_2O and 12 p.p.b.v. NO_2. For product detection and identification, 5 compound-specific 40-cm-long glass denuders (4 mm inner diameter) were designed as coils around the γ-ray detectors (5.5 cm diameter). The first was coated with sodium chloride (HNO_3 detection), the second and third with a sodium carbonate/glycerol mixture (HNO_2), the fourth with a triethanolamine/guaiacol mixture (NO_2), and the fifth with cobalt(II/III) oxide (NO). For HNO_2, the two denuders with the same coating in series allowed a correction for interference by NO_2. The γ-ray activities measured at the denuders (NO_2 and HNO_2) and at the filter (N_{chem}) were converted to fluxes of molecules into each trap using the 9.96-min half-life of ^{13}N. In each experiment, the background effect caused by the reaction of NO_2 to HNO_2 at the glass walls of the flow reactor (reaction (1)) was measured before and after the soot particles were present.

Significant chemical effects of soot from both natural and anthropogenic sources in the atmosphere have been postulated[6], but previous experimental studies on the reaction of NO_2 with soot to form NO or HNO_2 were mostly performed with bulk carbonaceous samples in vacuum or with very high NO_2 concentrations (refs 7–9). That is, the reaction has not yet been studied under realistic conditions with respect to the physical and chemical characteristics of the soot surface, pressure, NO_2 concentration and humidity. The present study addresses this shortcoming by making use of the short-lived radioactive isotope ^{13}N (half-life 9.96 min) as a tracer[10,11] to monitor the effects of soot aerosol on NO and HNO_2 formation under conditions typical for the polluted troposphere.

The interaction between NO_2 and soot particles was studied in a flow reactor at 22 °C, ambient pressure and 50% relative humidity. A flow of inert gas and oxygen containing 12 p.p.b.v. NO_2 (enriched with $^{13}NO_2$) and a flow of an air/inert-gas mixture containing suspended soot particles, both equilibrated to a relative humidity of 50%, were mixed in the reaction vessel. The extent of the interaction between NO_2 and soot aerosol was monitored by combining ^{13}N measurements with the denuder technique[11,12] which differentiates between chemical compounds according to their reactivity. This set-up allows the simultaneous and online measurement of nitric acid (HNO_3), HNO_2, NO_2, NO and particle-bound products (chemisorbed nitrogen, N_{chem}) in the gas leaving the reaction vessel.

The soot aerosol was monitored online by differential mobility analysis[13] giving concentrations of typically 2×10^6 particles cm^{-3} with an average diameter of 70 nm and S/V of 3×10^{-4} cm^{-1}. This size distribution agrees with measured black carbon size distributions in the polluted PBL[14]. For non-sperhical particles, the equivalent mobility diameter, which is the diameter of the sphere with the same mobility, is the preferred size parameter when mass transfer to agglomerated aerosol particles is considered[15]. The total surface area density derived with this technique for weighed samples of particles collected on a filter was 300 $m^2 g^{-1}$. Carbon and oxygen chemistry on the surface of the soot particles was checked by X-ray photoelectron spectroscopy[16] which is sensitive to chemical bonding of the elements present in the uppermost layers of the surface. The spectra in the C(1*s*) and O(2*p*) region were similar to samples directly collected from diesel exhaust, indicating that the soot particles used in the present experiments expose similar C–O and C–H functionalities as fresh diesel soot particles. Thermal analysis[17] showed that they contained 40% organic and 60% elemental carbon which again is typical for soot from combustion exhaust[18]. The soot particles used here thus seem to adequately represent the chemical and physical characteristics of fresh soot emitted to the atmosphere by combustion sources, while still being suitable for a very sensitive laboratory aerosol study.

Figure 1 shows the fluxes of HNO_2, NO_2 and N_{chem} that are detected 20 s after the gas flows containing the reagents have mixed in the reaction vessel. In the absence of soot aerosol, the NO_2, HNO_2 and N_{chem} fluxes are fairly constant, with only relatively small amounts of HNO_2 and N_{chem} being formed. In the presence of soot aerosol, however, the HNO_2 flux increases significantly, thus providing direct evidence for substantial heterogeneous HNO_2 production. To obtain an estimate for the rate of production, HNO_2 concentrations were inferred from the measured fluxes and monitored as a function of reaction time (the time that has elapsed after the reagent flows have mixed in the reaction vessel). Figure 2 shows data obtained in the presence of 12 p.p.b.v. NO_2 and for reaction times ranging from 5 to 155 s. The data indicate that HNO_2 is produced under these conditions at a rate of 1.0×10^{12} molecules per s per cm^2 aerosol surface. The data also imply that HNO_2 formation is much more rapid within the first 5 s after the reaction has been initiated. With a modified experimental set-up that improved the time-resolution of the system, a HNO_2 production rate of 3.3×10^{13} molecules per s per cm^2 aerosol surface was derived on this time scale (Fig. 3). The probability that a collision between a NO_2 molecule and a soot particle will result in the formation of HNO_2 is known as the reaction probability γ. The data shown in Figs 2 and 3 yield values of 1.1×10^{-2} and 3.3×10^{-4}, respectively, for this parameter. The reaction probability of reaction (1) at 50% relative humidity, in contrast, is only 3×10^{-9} as inferred from laboratory studies on other surfaces (ref. 1), thus indicating that the interaction between NO_2 and the soot aerosols studied here leads to a HNO_2 formation rate that is about 5 to 7 orders of magnitude faster.

The previously suggested heterogeneous process (reaction (1)) (ref. 19) predicts the formation of equal amounts of HNO_2 and HNO_3, but we were not able to detect the latter as a product of the NO_2/soot interaction. Although it is conceivable that HNO_3 remains adsorbed to the particle surface, or that it decomposes into NO (ref. 8), these processes are not likely to explain the observed absence of significant HNO_3 formation: the concentration of particle-bound N-species we measured was two orders of magnitude lower than the amount of HNO_2 formed while NO formation was below the detection limit (1‰ of the NO_2 concentration) of our system. These observations imply that, instead of the disproportionation of N(IV) into equal amounts of N(V) and N(III) species, a net reduction of N(IV) to N(III) is taking place at low NO_2 concentrations. Although previous studies[8,9,19] have already indicated that NO_2 may be reduced on soot to form NO or N_2O, our observations suggest the existence of an additional reaction channel (reaction (2)) that results in HNO_2 formation.

$$NO_2 + red_{ads} \rightarrow HNO_2(g) + ox_{ads} \quad (2)$$

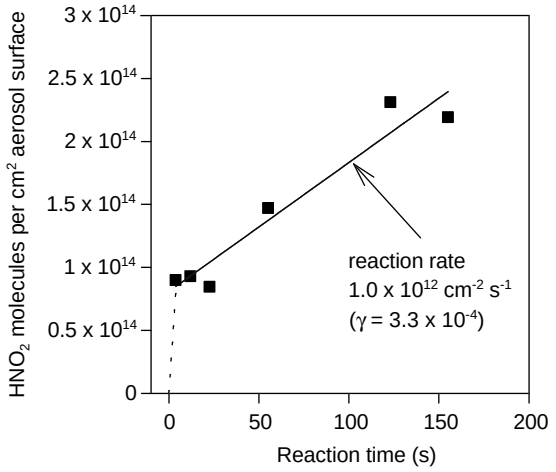

Figure 2 HNO_2 concentrations, normalized to total particle surface area, as a function of reaction time. The data were obtained using the system described in Fig. 1. The reaction times could be varied between 5 and 20 s by using a movable inlet for the introduction of the NO_2 gas flow, thereby achieving a range of distances (and hence reaction times) between the mixing of the two gas flows and the detection of reaction products. The longer reaction times of 50 s, 114 s and 155 s were achieved by using 3 larger reaction vessels with fixed inlets and diameters of 4 cm, 6 cm and 7 cm. After subtraction of the background signals (obtained as in Fig. 1) for each experiment, the HNO_2 concentration was calculated from the net flux of ^{13}N molecules into the denuder and the gas flow rate of 16.7 $cm^3 s^{-1}$ through the denuders, and assuming constant ratios of labelled to non-labelled molecules for all species. HNO_2 formation is normalized to the total particle surface area calculated by integration of the size spectra obtained with the differential mobility analyser during each experiment. The reaction probability, γ, was calculated from the linear regression of the data (solid line) and the gas kinetic flux of NO_2 molecules to the particle surface. The dashed line indicates the fast onset of HNO_2 production at times below 5 s.

Reaction (2) is presented as a net reaction without explicitly stating its elementary steps, where red_{ads} and ox_{ads} denote a reduced and an oxidized site on the soot surface, respectively. The electron transfer properties of the carbon-oxygen functionalities typical for soot[7] are not sufficiently understood to allow a specific assignment of the different kinetic regimes found (Figs 2 and 3). Our results clearly indicate that HNO_2 forms much more efficiently than NO. The slow NO formation was quantified in our earlier aerosol study[11], and is in contrast to reports on bulk amorphous carbon samples giving a reaction probability of 10^{-1} for NO formation[8,9].

We performed several tests to explore the sensitivity of reaction (2) to oxygen, ozone and humidity. Exposure of the soot particles to NO_x-free air of 50% relative humidity for 1 min before the reaction with NO_2 did not change the HNO_2 output, suggesting that oxygen does not compete with NO_2 for reducing groups on the soot surface. A corresponding pretreatment of the particles with 200 p.p.b.v. ozone (O_3) for 2 min reduced HNO_2 formation by 40%. On the other hand, HNO_2 formation was not affected when the particles were exposed to 12 p.p.b.v. NO_2 and up to 200 p.p.b.v. O_3 at the same time, indicating that ozone will not significantly influence HNO_2 formation on soot in the atmosphere in the short term. Whereas reaction (1) was found to be very sensitive to the water concentration[19], in our experiments, at 0.5% relative humidity the formation of HNO_2 was (within the experimental uncertainty) the same as at 60%. Even at these low humidities, the gas-phase concentration of H_2O is large enough to allow some soot functionalities (such as carboxyl groups) to be hydrated or to lead to the presence of physisorbed H_2O (ref. 8).

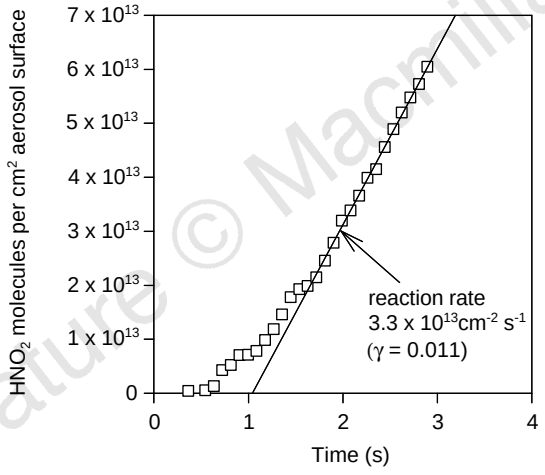

Figure 3 HNO_2 formation on soot particles at 12 p.p.b.v. NO_2 and 50% relative humidity at reaction times below 3 s. The aerosol and the NO_2 flows were mixed at the inlet of a 1-m-long tube (0.8 cm inner diameter) coated with a sodium carbonate/glycerol mixture which retains all HNO_2 molecules diffusing to the tube wall. The total flow rate was 16.7 $cm^3 s^{-1}$. The amount of ^{13}N arriving at each tube segment of 3 cm length was measured with a γ-ray detector after 30 min. First, the background signal caused by NO_2 flowing through the tube was measured without the soot particles in the gas stream. For the plot, the difference of the signals with and without the aerosol at each segment was integrated along the tube and normalized to the particle surface area in the gas stream. The first 30 cm were not used for the kinetic analysis, because mixing of the two gas flows occurs here. Under the conditions chosen, the diffusion to the wall was faster than production of new HNO_2 molecules, so that no correction was applied to the data. The diffusion causes a slight delay of the response at the wall (corresponding to 0.5 s on the time scale) which does not affect the slope analysed for the calculation of the reaction probability, γ. This experiment differs from the experiments shown in Figs 1 and 2 in that HNO_2 is continuously removed from the gas phase during the NO_2/aerosol interaction. The data shown in Figs 1 and 2, in contrast, illustrate the formation rates that are obtained when HNO_2 is removed at the end of a fixed reaction time.

Urban air masses typically contain[14] 10 $\mu g\,m^{-3}$ soot, which corresponds to an aerosol surface to volume ratio of $3 \times 10^{-5}\,cm^{-1}$ (assuming a specific surface area identical to that measured for our model aerosol). Using these values and the reaction probabilities obtained from our experiments, we calculate night-time NO_2 conversion rates of $3.7 \times 10^{-3}\,s^{-1}$ and $1.1 \times 10^{-4}\,s^{-1}$ at 10 p.p.b.v. NO_2 and 50% relative humidity for the two different kinetic regimes. The long-term kinetics of reaction (2) could not be studied due to the low half-life of ^{13}N, but already within the short timescale of our study (155 s), the observed HNO_2 production (3×10^{14} molecules cm^{-2}) builds up 0.3 p.p.b.v. HNO_2. Extrapolated to longer timescales (10 h night-time) or lower soot loadings (0.1 to 1 $\mu g\,m^{-3}$ for rural areas), concentrations typical for the PBL are reached (0.01 to 10 p.p.b.v.; ref. 1). After high HNO_2 levels have built up during the night, the yield of OH radicals from its photolysis in the morning (maximum, $3 \times 10^7\,cm^{-3}\,s^{-1}$ for 1 p.p.b.v. HNO_2) exceeds other photochemical sources of OH radical which reach their maximum around noon (typically $10^7\,cm^{-3}\,s^{-1}$)[4]. Hence, the high reactivity of soot particles in the polluted PBL may be one of the main factors in initiating daytime photochemistry. The suggested HNO_2 production on soot particles may also play an important role in less polluted rural areas where a fast HNO_2 production process has been postulated to bring measured HNO_2 values and a photochemical model into agreement[21].

Soot particles have been suggested[6,22] to affect the nitrogen oxide chemistry of the remote troposphere and stratosphere by reducing HNO_3 and NO_2 to NO. We find, in contrast, that the reduction of NO_2 in polluted air masses leads to at least two orders of magnitude more HNO_2 than NO. Furthermore, the HNO_2 that has been built up throughout the night is photolysed the next morning to form the strongly oxidizing OH radical, and it therefore seems unlikely that heterogeneous reactions on soot particles result in a net reduction of the nitrogen oxide species in polluted air. The process may even have a net oxidizing effect on nitrogen oxides, and hence on ozone in the PBL, but in the absence of detailed model calculations a reliable assessment of its overall effect is not yet possible.

Soot particles are ubiquitous throughout the atmosphere[23], including the upper troposphere and lower stratosphere[24]. During their long residence times in the atmosphere they undergo a variety of ageing processes, such as the proposed reaction with NO_2, reactions with other oxidants, and coating with sulphuric acid or secondary organic material. On aged soot, the HNO_2 formation process suggested here may only be significant if surface species oxidized by reaction (2) are recycled. SO_2 could be a good candidate to maintain such a mechanism[25], and solar radiation could affect the fate of the oxidized surface by inducing decarboxylation[26] or other photon-induced formation of new surface radicals[27]. Although HNO_2 formation on soot in remote areas of the PBL has already been suggested (ref. 28) to mediate the nitration of hydrocarbon trace species, a reliable assessment of the overall effects of this process requires further studies of the heterogeneous chemistry of aged soot and its associated secondary constituents. □

Received 18 July 1997; accepted 23 June 1998.

1. Lammel, G. & Cape, J. N. Nitrous acid and nitrite in the atmosphere. *Chem. Soc. Rev.* 361–369 (1996).
2. Kitto, A.-M. N. & Harrison, R. M. Nitrous and nitric acid measurements at sites in south-east England. *Atmos. Environ. A* **26,** 235–241 (1992).
3. Andrés-Hernandez, M. D., Notholt, J., Hjorth, J. & Schrems, O. A DOAS study on the origin of nitrous acid at urban and non-urban sites. *Atmos. Environ.* **30,** 175–180 (1996).
4. Harrison, R. M., Peak, J. D. & Collins, G. M. Tropospheric cycle of nitrous acid. *J. Geophys. Res.* **101,** 14429–14439 (1996).
5. Kirchstetter, T. W., Harley, R. A. & Littlejohn, D. Measurement of nitrous acid in motor vehicle exhaust. *Environ. Sci. Technol.* **30,** 2843–2849 (1996).
6. Lary, D. J. *et al.* Carbon aerosols and atmospheric photochemistry. *J. Geophys. Res.* **102,** 3671–3682 (1997).
7. Akhter, M. S., Chughtai, A. R. & Smith, D. M. The structure of hexane soot I: Spectroscopic studies. *Appl. Spectrosc.* **39,** 143–153 (1985).
8. Rogaski, C. A., Golden, D. M. & Williams, L. R. Reactive uptake and hydration experiments on amorphous carbon treated with NO_2, SO_2, O_3, HNO_3, and H_2SO_4. *Geophys. Res. Lett.* **24,** 381–384 (1997).
9. Tabor, K., Gutzwiller, L. & Rossi, M. J. Heterogeneous chemical kinetics of NO_2 on amorphous carbon at ambient temperature. *J. Phys. Chem.* **98,** 6172–6175 (1994).

10. Baltensperger, U. *et al.* Use of positron-emitting ^{13}N for studies of the selective reduction of NO by NH_3 over vanadia/titania catalyst at very low reactant concentrations. *J. Phys. Chem.* **97,** 12325–12330 (1993).
11. Kalberer, M. *et al.* Heterogeneous chemical processing of $^{13}NO_2$ by monodisperse carbon aerosols at very low concentrations. *J. Phys. Chem.* **100,** 15487–15493 (1996).
12. Allegrini, I. *et al.* Annular denuder method for sampling reactive gases and aerosols in the atmosphere. *Sci. Tot. Environ.* **67,** 1–16 (1987).
13. Liu, B. Y. H. & Pui, D. Y. H. A submicron aerosol standard and the primary absolute calibration of the condensation nuclei counter. *J. Colloid Interface Sci.* **47,** 155–171 (1974).
14. Berner, A. *et al.* Modal character of atmospheric black carbon size distributions. *J. Geophys. Res.* **101,** 19559–19565 (1996).
15. Rogak, S. N., Baltensperger, U. & Flagan, R. C. Measurement of mass transfer to agglomerate aerosols. *Aerosol Sci. Technol.* **14,** 447–458 (1991).
16. Wild, U., Pfänder, N. & Schlögl, R. Species analysis of automative carbon particles: application of XPS for integral analysis of filter samles. *Fresenius J. Anal. Chem.* **357,** 420–428 (1997).
17. Cachier, H., Bremond, M.-P. & Buat-Ménard, P. Determination of atmospheric soot carbon with a simple thermal method. *Tellus B* **41,** 379–390 (1989).
18. Burtscher, H., Künzel, S., Hüglin, Ch. Characterization of particles in combustion engine exhaust. *J. Aerosol Sci.* **29,** 389–396 (1998).
19. Chughtai, A. R., Welch, J. W. F., Akhter, M. S. & Smith, D. M. Spectroscopic study of gaseous products of soot—oxides of nitrogen/water reactions. *Appl. Spectrosc.* **44,** 294–298 (1990).
20. Febo, A. & Perrino, C. Prediction and experimental evidence for high air concentration of nitrous acid in indoor environments. *Atmos. Environ. A* **25,** 1055–1061 (1991).
21. Staffelbach, T., Neftel, A. & Horowitz, L. W. Photochemical oxidant formation over southern Switzerland 2. Model results. *J. Geophys. Res.* **102,** 23363–23373 (1997).
22. Haugloustaine, D. A., Ridley, B. A., Solomon, S., Hess, P. G. & Madronich, S. HNO_3/NO_x ratio in the remote troposphere during MLOPEX2: Evidence for nitric acid reduction on carbonaceous aerosols? *Geophys. Res. Lett.* **23,** 2609–2612 (1996).
23. Liousse, C. *et al.* A global three-dimensional model study of carbonaceous aerosols. *J. Geophys. Res.* **101,** 19411–19432 (1996).
24. Blake, D. F. & Kato, K. Latitudinal distribution of black carbon soot in the upper troposphere and lower stratosphere. *J. Geophys. Res.* **100,** 7195–7202 (1995).
25. De Santis, F. & Allegrini, I. Heterogeneous reactions of SO_2 and NO_2 on carbonaceous surfaces. *Atmos. Environ.* **26,** 3061–3064 (1992).
26. Smith, D. M. & Chughtai, A. R. Photochemical effects in the heterogeneous reaction of soot with ozone at low concentrations. *J. Atmos. Chem.* **26,** 77–91 (1997).
27. Weschler, C. J., Mandich, M. L. & Graedel, T. E. Speciation, photosensitivity, and reactions of transition metal ions in atmospheric droplets. *J. Geophys. Res.* **91,** 5189–5204 (1986).
28. Ciccioli, P., Cecinato, A., Brancaleoni, E., Frattoni, M. & Zacchei, P. Formation and transport of 2-nitrofluoranthene and 2-nitropyrene of photochemical origin in the troposphere. *J. Geophys. Res.* **101,** 19567–19580 (1996).

Acknowledgements. The stable proton beam from the Philips Cyclotron necessary for ^{13}N production was provided by the staff of the Accelerator Facilities at Paul Scherrer Institute; V. Lavanchy, B. Schnyder and R. Koetz performed the offline analysis of soot samples. Contributions from S. Nyeki, C. Zellweger, E. Weingartner, P. Zimmermann and B. Eichler were greatly appreciated.

Correspondence and requests for materials should be addressed to M.A. (e-mail: markus.ammann@psi.ch).

Mantle discontinuities and temperature under the North American continental keel

Aibing Li*, Karen M. Fischer*, Michael E. Wysession† & Timothy J. Clarke‡

* *Department of Geological Sciences, Brown University, Providence, Rhode Island 02912, USA*
† *Department of Earth and Planetary Sciences, Washington University, St Louis, Missouri 63130, USA*
‡ *Department of Earth and Environmental Sciences, New Mexico Institute of Mining and Technology, Socorro, New Mexico 87801, USA*

A ubiquitous feature of upper-mantle seismic velocity models has been the presence of high-velocity 'keels' beneath stable continental interiors[1–5]. Uncertainty remains, however, regarding the maximum depth to which continental keels extend, the degree to which they have cooled the mantle that surrounds them and their role in mantle flow. Here we investigate thermal anomalies across the eastern margin of the North American continental keel by imaging the seismic discontinuities at depths of 410 and 660 km with compressional-to-shear converted waves recorded by a 1,500-km-long seismometer deployment in the eastern United States. The thickness of the transition zone (the region nominally between depths of 410 and 660 km) and the depth to the '410-km' discontinuity indicate that cold keel material and sub-keel downwellings must be largely confined to the upper mantle and may impinge on the transition zone only in localized regions and with thermal anomalies of less than ~150 K. A 20-km depression of the '660-km' discontinuity to the south of the westernmost stations coincides with a region of fast velocity in the deep transition zone[2] and may be associated with the remnants of the subducted Farallon plate[1,2,4].

Discontinuities in seismic velocity have been observed at depths of roughly 410 km and 660 km in the Earth's mantle (hereafter referred to as the '410' and '660'). These discontinuities mark the upper and lower boundaries of the mantle transition zone, and are generally interpreted as mineral phase transitions from α-olivine to β-spinel, and from γ-spinel to perovskite+magnesiowüstite, respectively. The Clapeyron slopes of the equilibrium phase boundaries indicate that the depth of the '410' discontinuity should be deflected upwards in regions of colder temperature, whereas the '660' should be deflected downwards. The topography of the '410' and '660' discontinuities can therefore provide information about thermal structure in the mantle transition zone.

Knowledge of transition-zone temperatures below continental regions is important in understanding the role of continental keels in mantle flow. High-velocity keels have been imaged beneath stable continental interiors to depths of 300 km or more, but although keel velocity anomalies are strongest in the upper mantle, their maximum depth extent has not been clearly resolved[1–7]. Some studies have argued that continental keels are neutrally buoyant features in which positive density anomalies due to cold temperature are roughly balanced by negative density anomalies due to chemical depletion[5,8,9]. However, other investigations have concluded that keels are in fact anomalously dense, and should be associated with broad zones of strong mantle downwelling[10,11]. In addition, even if keels are neutrally buoyant, the presence of these cold anomalies in the mantle over timescales of 1–2 Gyr may produce small-scale convective instabilities at the base of the keel[12]. Transition-zone discontinuity topography can constrain the maximum depth extent of the cold keel itself, and if downwelling is occurring, the strength and wavelength of these convective instabilities.

Seismological investigations have reached a variety of conclusions regarding transition-zone discontinuity topography across continental

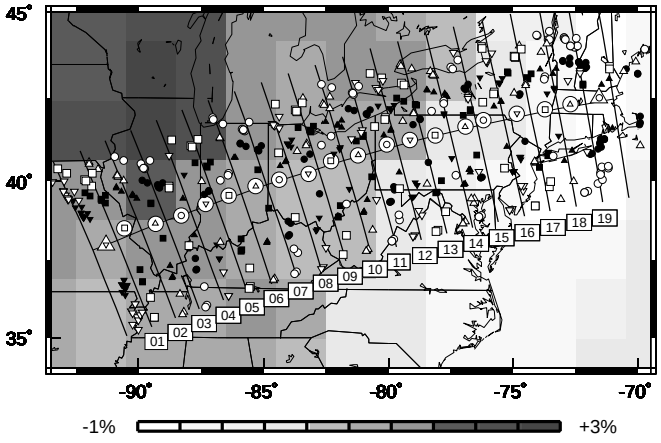

Figure 1 Ps conversion points at depths of 410 km (small black symbols) and 660 km (small white symbols) plotted on S-wave velocity anomalies from Grand[2] for depths of 175–250 km. Temporary stations of the MOMA array are shown as larger white circles, permanent stations HRV and CCM are denoted by larger white triangles, and the small symbol plotted at each station corresponds to the symbol of nearby Ps conversions recorded by that station. Bin numbers are given below the centre of each bin. The margin of the continental keel is marked by the west-to-east decrease in velocity anomaly, and is well sampled by Ps conversions from depths near 410 and 660 km.